41st Aerospace Sciences Meeting and Exhibit
6-9 January 2003, Reno, Nevada

AIAA 2003-548

INITIAL EVALUATION OF AN ALGEBRAIC REYNOLDS STRESS MODEL FOR COMPRESSIBLE TURBULENT SHEAR FLOWS

Dennis A. Yoder*
National Aeronautics and Space Administration
Glenn Research Center
Cleveland, Ohio

Abstract

An explicit algebraic Reynolds stress model originally formulated for incompressible flows has been implemented in the WIND Navier-Stokes flow solver. Validation results are presented for an attached incompressible turbulent boundary layer and indicate good agreement with experimental data, though the model lacks the near wall terms necessary to reproduce details such as the sharp rise in turbulent kinetic energy outside of the viscous sublayer. The model is then applied to a compressible mixing layer and a supersonic elliptic jet flow. Comparisons with two-equation eddy viscosity models available in WIND indicate that the algebraic stress model appears to better replicate the shape of the mean velocity profiles in both cases. The primary deficiency of the model is that it slightly underpredicts the rate of mixing. In all of these cases, the algebraic stress model demonstrates its unique ability to predict an anisotropic distribution of the turbulence intensities.

Nomenclature

A_{exit}	nozzle exit area
b	mixing layer thickness between transverse locations where $\widetilde{u} = \widetilde{u}_1 - 0.1\Delta\widetilde{u}$ and $\widetilde{u} = \widetilde{u}_2 + 0.1\Delta\widetilde{u}$
b_{ij}	Reynolds stress anisotropy tensor, $b_{ij} = \overline{\rho u_i'' u_j''}/2\bar{\rho}k - \delta_{ij}/3$
C_f	local skin friction coefficient
D_{eq}	equivalent diameter, $D_{eq} = 2\sqrt{A_{exit}/\pi}$
k	turbulent kinetic energy, $\bar{\rho}k = \overline{\rho u_i'' u_j''}$
M	Mach number
M_c	Convective Mach number, $M_c = (\widetilde{u}_1 - \widetilde{u}_2)\,/\,(a_1 + a_2)$ where a is the speed of sound
$\mathcal{P}$	production of turbulent kinetic energy
P	pressure
S_{ij}	strain rate tensor, $S_{ij} = (u_{i,j} + u_{j,i})/2$
R_{ij}	rotation tensor, $R_{ij} = (u_{i,j} - u_{j,i})/2$
Re_x	Reynolds number based on x
T	temperature
u	velocity
U_{jet}	ideal jet exit velocity, $U_{jet} = \sqrt{\left(\frac{2\gamma}{\gamma-1}\right) R_{gas} T_t \left[1 - \left(\frac{P_t}{P_\infty}\right)^{(1-\gamma)/\gamma}\right]}$
u_τ	friction velocity, $u_\tau = \sqrt{\tau_{wall}/\rho_{wall}}$
x, y, z	spatial coordinates
y_0	mixing layer centerline (midpoint between transverse locations where $\widetilde{u} = \widetilde{u}_1 - 0.1\Delta\widetilde{u}$ and $\widetilde{u} = \widetilde{u}_2 + 0.1\Delta\widetilde{u}$)
y^+	sublayer scaled wall distance, $y^+ = y u_\tau/\nu_L$
$\Delta\widetilde{u}$	freestream velocity difference, $\Delta\widetilde{u} = \widetilde{u}_1 - \widetilde{u}_2$
δ	boundary layer thickness
δ_{ij}	Kronecker delta
ϵ	turbulent dissipation rate
κ	Kármán constant, $\kappa = 0.41$
μ	kinematic viscosity
ν	dynamic viscosity
Π_{ij}^D	deviatoric pressure strain correlation tensor $\Pi_{ij}^D = \overline{P'\left(\frac{\partial u_i''}{\partial x_j} + \frac{\partial u_j''}{\partial x_i}\right)} - \frac{2}{3}\overline{P'\frac{\partial u_k''}{\partial x_k}\delta_{ij}}$
ρ	density
τ_T	turbulent time scale
τ_{ij}	viscous stress tensor
τ_{wall}	wall shear stress
ω	specific dissipation rate

subscripts/superscripts

∞	freestream
L	laminar
T	turbulent
t	total
1	high-speed stream
2	low-speed stream

accents

$\overline{u}_j$	Reynolds-averaged mean velocity
u_j'	Reynolds fluctuating velocity
$\widetilde{u}_j$	Favre-averaged mean velocity
u_j''	Favre fluctuating velocity

*AIAA Member

Introduction

Previous work[1] conducted at the NASA Glenn Research Center and by industry partners has indicated deficiencies of eddy viscosity turbulence models when applied to compressible, shear-dominated flowfields which have flow conditions similar to those encountered in the exhaust nozzles of subsonic commercial aircraft and proposed future supersonic vehicles. Even with the inclusion of additional terms to try to account for the round-jet/plane-jet anomaly and compressibility effects, these models still fail to provide agreement with experimental data for shear layer spreading rates and jet centerline velocity decay. In addition, there is growing interest in the aeroacoustics community in predicting not only the turbulent kinetic energy, but also the individual Reynolds normal stresses which form the components of k and using these values as inputs to empirical noise prediction codes.[2] This has lead to the pursuit of higher-order turbulence models such as algebraic Reynolds stress models.

Algebraic stress models (ASMs) are derived from a simplified form of the Reynolds stress transport equation. These models provide for improved physical modeling of turbulence over traditional two-equation eddy-viscosity models and incur a relatively low cost compared to other alternatives such as full Reynolds stress models. From a computational standpoint, *explicit* ASMs (EASMs) are preferred over *implicit* formulations because: (1) explicit formulations provide direct expressions for each of the Reynolds stresses without having to sub-iterate on a system of non-linear algebraic equations, and (2) implicit formulations, when solved iteratively can result in non-unique solutions and singularities which inhibit numerical convergence.[3]

EASMs are generally written in terms of the turbulent kinetic energy (k), turbulent dissipation rate (ϵ), mean strain-rate tensor ($\widetilde{S}_{ij}$), and mean rotation tensor ($\widetilde{R}_{ij}$). The resultant expression used to calculate the turbulent stresses resembles that used with typical two-equation eddy viscosity models with additional terms that are nonlinear in $\widetilde{S}_{ij}$ and $\widetilde{R}_{ij}$. However, unlike non-linear eddy-viscosity models, which can have somewhat arbitrary formulations for the higher-order terms, the resulting expression for the stresses in an ASM follows directly from simplifications made to the Reynolds stress transport equation. Therefore while the link between the ASM and $k-\epsilon$ model may appear to be weak and involve merely replacing the Boussinesq approximation with a slightly more complicated formula, these ASMs are more closely aligned with full Reynolds stress models. In addition, these ASMs are calibrated for use with a particular underlying $k-\epsilon$ model, which means one cannot simply swap $k-\epsilon$ models as when using the Boussinesq expression.

Rodi[4] was among the first to propose an algebraic Reynolds stress model. Since the convection and diffusion terms make the Reynolds stress transport equation a differential equation, he proposed that these terms be related to the convection and diffusion of the turbulent kinetic energy. The key to this simplification is the assumption that derivatives of the anisotropy tensor b_{ij} are small and can be neglected. The transport equation for the turbulent kinetic energy equation is then used to replace the convection and diffusion of turbulent kinetic energy with the production and dissipation of k. This results in a nonlinear algebraic equation for the Reynolds stresses. Unfortunately, Rodi's model is an implicit formulation subject to the undesirable numerical behavior previously described.

Building upon Rodi's work, Pope[5] presented a methodology based on the use of integrity bases from linear algebra which resulted in semi-explicit relations for the turbulent stresses. Gatski and Speziale[6] extended this technique to three-dimensional flows in non-inertial frames by treating the ratio of production to dissipation of turbulent kinetic energy as a known quantity and linearizing the problem.

Girimaji[7] demonstrated that if one does not linearize about the equilibrium value of production to dissipation, it is possible to reduce the non-linear problem to the solution of a single cubic equation for one of the closure coefficients. In solving the cubic equation, Girimaji's selection of the proper root is governed by the argument that the closure coefficient must be a continuous function.

Instead of using the continuity arguments of Girimaji to provide an explicit solution to the algebraic Reynolds stress equations, Jongen and Gatski[8] use the limiting behavior of a dynamic system to show that the correct root to be used is the one with the lowest real part. This approach has been used by Rumsey and Gatski[9,10] in implementing $k-\epsilon$ and $k-\omega$ based EASMs in the CFL3D code and is the basis upon which the WIND EASM has been formulated. Because $k-\epsilon$ models have historically performed better than $k-\omega$ models for computing free shear flows, the $k-\epsilon$ ASM formulation of reference 9 is the focus of this investigation.

The goal of the present study is to implement this explicit algebraic stress model in WIND[11,12] and determine its level of accuracy relative to linear two-equation eddy viscosity models in predicting basic shear flows which are have flow characteristics similar to those encountered in aircraft engine exhaust nozzles. In order to provide an equivalent comparison between models, no explicit corrections for compressibility effects, such as those for pressure-dilatation or dilatation dissipation, have been used. Appropriate extension of the ASM formulation for compressible flows shall be the subject of future work.

ASM Formulation

In the ASM formulation, the turbulent stress tensor is computed from

$$\tau_{ij}^{T} = -\overline{\rho u_i'' u_j''} \tag{1}$$

$$\begin{aligned} &= -\frac{2}{3}\bar{\rho}k\delta_{ij} + 2\mu_T^*\Big[\quad \Big(\widetilde{S}_{ij} - \tfrac{1}{3}\widetilde{S}_{kk}\delta_{ij}\Big) \\ &\qquad + F_1\Big(\widetilde{S}_{ik}\widetilde{R}_{kj} - \widetilde{R}_{ik}\widetilde{S}_{kj}\Big) \\ &\qquad + F_2\Big(\widetilde{S}_{ik}\widetilde{S}_{kj} - \tfrac{1}{3}\widetilde{S}_{kl}\widetilde{S}_{kl}\delta_{ij}\Big)\Big] \end{aligned} \tag{2}$$

where the first line of Eq. (2) is identical to the expression obtained using the Boussinesq approximation. The coefficients multiplying the nonlinear terms are given by

$$F_1 = \quad a_2 a_4 \tag{3}$$

$$F_2 = -2a_3 a_4 \tag{4}$$

The "nonlinear" eddy viscosity expression used is

$$\mu_T^* = C_\mu^* \bar{\rho} k \tau_T \tag{5}$$

where the turbulent time scale is given by

$$\tau_T = \frac{k}{\epsilon} = \frac{1}{\omega} \tag{6}$$

Note that the specific dissipation rate ω used above differs from that used in the $k-\omega$ formulations of references 13 and 14 in that it does not contain the embedded constant $\beta^* = 0.09$. The coefficient C_μ^* varies throughout the flowfield and is computed by solving the following cubic equation.

$$\left(-C_\mu^*\right)^3 + p\left(-C_\mu^*\right)^2 + q\left(-C_\mu^*\right) + r = 0 \tag{7}$$

where

$$p = -\gamma_1^* / \left(\eta_1^2 \gamma_0^*\right) \tag{8}$$

$$q = \frac{\left(\gamma_1^{*2} - 2\eta_1^2\gamma_0^* a_1 - \frac{2}{3}\eta_1^2 a_3^2 + 2\eta_2^2 a_2^2\right)}{\left(2\eta_1^2\gamma_0^*\right)^2} \tag{9}$$

$$r = \gamma_1^* a_1 / \left(2\eta_1^2\gamma_0^*\right)^2 \tag{10}$$

$$\eta_1^2 = \tau_T^2 \widetilde{S}_{ij}\widetilde{S}_{ij} \tag{11}$$

$$\eta_2^2 = \tau_T^2 \widetilde{R}_{ij}\widetilde{R}_{ij} \tag{12}$$

$$\gamma_0^* = C_1^1/2 \tag{13}$$

$$\gamma_1^* = \frac{C_1^0}{2} + \frac{C_{\epsilon 2} - C_{\epsilon 1}}{C_{\epsilon 1} - 1} \tag{14}$$

$$a_1 = \frac{2}{3} - \frac{C_2}{2} \tag{15}$$

$$a_2 = 1 - \frac{C_4}{2} \tag{16}$$

$$a_3 = 1 - \frac{C_3}{2} \tag{17}$$

$$a_4 = \frac{\tau_T}{\gamma_1^* + 2\gamma_0^* C_\mu^* \eta_1^2} \tag{18}$$

The coefficients C_1 through C_4 follow from the choice of model used for the deviatoric pressure-strain correlation tensor. The following quasi-linear expression is commonly used.

$$\begin{aligned} \frac{\Pi_{ij}^D}{\bar{\rho}\epsilon} &= -\left(C_1^0 + C_1^1\frac{\mathcal{P}}{\bar{\rho}\epsilon}\right) b_{ij} + C_2\frac{k}{\epsilon}\left(\widetilde{S}_{ij} - \frac{1}{3}\widetilde{S}_{kk}\delta_{ij}\right) \\ &\quad + C_3\frac{k}{\epsilon}\left(b_{ik}\widetilde{S}_{jk} + b_{jk}\widetilde{S}_{ik} - \frac{2}{3}b_{mn}\widetilde{S}_{mn}\delta_{ij}\right) \\ &\quad + C_4\frac{k}{\epsilon}\left(b_{ik}\widetilde{R}_{jk} + b_{jk}\widetilde{R}_{ik}\right) \end{aligned} \tag{19}$$

Speziale, Sarkar and Gatski[15] suggest the following values for the coefficients.

$$\begin{aligned} C_1^0 &= 3.4 \qquad C_2 = 0.36 \qquad C_4 = 0.4 \\ C_1^1 &= 1.8 \qquad C_3 = 1.25 \end{aligned} \tag{20}$$

The coefficients $C_{\epsilon 1}$ and $C_{\epsilon 2}$ used in computing γ_1^* are obtained from the underlying $k-\epsilon$ model used.

The following procedure is used to obtain the root to Eq. (7) which has the lowest real part:
If $\eta_1^2 < 10^{-6}$, then the degenerate case of $\eta_1^2 \to 0$ is given by

$$-C_\mu^* = \frac{-\gamma_1^* a_1}{\gamma_1^{*2} + 2\eta_2^2 a_2^2} \tag{21}$$

Otherwise, define

$$a = q - \frac{p^2}{3} \tag{22}$$

$$b = \frac{2p^3 - 9pq + 27r}{27} \tag{23}$$

$$d = \frac{b^2}{4} + \frac{a^3}{27} \tag{24}$$

If $d \geq 0$, there will be one real and two complex conjugate roots. The one with the smallest real part

is computed from the following.

$$A = \left(-\frac{b}{2}+\sqrt{d}\right)^{1/3} \quad (25)$$

$$B = \left(-\frac{b}{2}-\sqrt{d}\right)^{1/3} \quad (26)$$

$$t_1 = -\frac{p}{3}+(A+B) \quad (27)$$

$$t_2 = -\frac{p}{3}-\frac{(A+B)}{2} \quad (28)$$

$$t_3 = t_2 \quad (29)$$

$$-C_\mu^* = \min\left[t_1; t_2\right] \quad (30)$$

Else ($d < 0$), there will be three real and unequal roots given by:

$$\theta = \arccos\left(-\frac{b}{2}\Big/\sqrt{-\frac{a^3}{27}}\right) \quad (31)$$

$$t_1 = -\frac{p}{3}+2\sqrt{-\frac{a}{3}}\cos\left(\frac{\theta}{3}\right) \quad (32)$$

$$t_2 = -\frac{p}{3}+2\sqrt{-\frac{a}{3}}\cos\left(\frac{\theta}{3}+\frac{2\pi}{3}\right) \quad (33)$$

$$t_3 = -\frac{p}{3}+2\sqrt{-\frac{a}{3}}\cos\left(\frac{\theta}{3}+\frac{4\pi}{3}\right) \quad (34)$$

$$-C_\mu^* = \min\left[t_1; t_2; t_3\right] \quad (35)$$

Using trigonometric arguments, one can show that t_2 will always be the root of choice in Eq. (35).

The value of C_μ^* computed using this procedure is limited by $C_\mu^* = \max\left(C_\mu^*, 0.0005\right)$ to ensure some level of turbulence. Within the flat plate boundary layer, C_μ^* varies from the typical $k-\epsilon$ value of 0.09 in the log layer to 0.18 in the sublayer and at the edge of the boundary layer. For the planar mixing layer case, C_μ^* is roughly 0.07 within the shear layer and 0.18 in either core stream.

$k-\epsilon$ Model

For the $k-\epsilon$ formulation of the ASM, the following additional equations are solved.

$$\rho\frac{Dk}{Dt} = \frac{\partial}{\partial x_j}\left[\left(\mu_L+\frac{\mu_T^*}{\sigma_k}\right)\frac{\partial k}{\partial x_j}\right]+\mathcal{P}-\rho\epsilon \quad (36)$$

$$\rho\frac{D\epsilon}{Dt} = \frac{\partial}{\partial x_j}\left[\left(\mu_L+\frac{\mu_T^*}{\sigma_\epsilon}\right)\frac{\partial \epsilon}{\partial x_j}\right] + C_{\epsilon 1}f_1\frac{\epsilon}{k}\mathcal{P}-C_{\epsilon 2}f_2\frac{\rho\epsilon^2}{k} \quad (37)$$

$$f_1 = 1.0 \quad (38)$$

$$f_2 = \left[1-\exp\left(-\frac{R_y}{10.8}\right)\right] \quad (39)$$

$$R_y = \sqrt{k}y/\nu_L \quad (40)$$

$$\kappa = 0.41 \quad (41)$$

$$C_\mu = 0.0885 \quad (42)$$

$$C_{\epsilon 1} = 1.44 \quad (43)$$

$$C_{\epsilon 2} = 1.83 \quad (44)$$

$$\sigma_k = 1.0 \quad (45)$$

$$\sigma_\epsilon = \frac{\kappa^2}{\sqrt{C_\mu}\left(C_{\epsilon 2}-C_{\epsilon 1}\right)} \approx 1.4489 \quad (46)$$

Wall Boundary Condition:

$$\tau_{ij}^T = 0 \quad \mu_T^* = 0 \quad k = 0 \quad \epsilon = 2\nu_L\left(\frac{\partial\sqrt{k}}{\partial y}\right)^2 \quad (47)$$

Production Term

Rumsey[10] suggests that the production of turbulent kinetic energy may be approximated by

$$\mathcal{P} = \tau_{ij}^T\frac{\partial\widetilde{u}_i}{\partial x_j} \approx 2\mu_T^*\widetilde{S}_{ij}\widetilde{S}_{ij} \quad (48)$$

which is exact for two-dimensional incompressible flow. This approximation has been included in the WIND implementation as an option and may be investigated at a later time. However, all of the ASM results presented herein were computed using the complete production term obtained by substituting the expression for τ_{ij}^T from Eq. (2) into Eq. (48).

Implementation

Implementation of the algebraic Reynolds stress model in WIND was accomplished by building upon the existing routines for solving the Chien $k-\epsilon$ equations. Details of that solution methodology are available in reference 16 and will not be repeated here. However, key modifications of this algorithm shall be outlined.

In order to accommodate the ASM into WIND, modifications were made to the mean-flow equations and the turbulent kinetic energy production term to use the expression for τ_{ij}^T from Eq. (2) rather than that from the Boussinesq approximation. Additional routines were added to handle the turbulence model source terms (namely those terms on the right hand side of Eqs. (36) and (37) excluding the diffusion terms), the enforcement of the wall boundary conditions listed in Eq. (47), and the solution of the cubic relation for C_μ^* given by Eq. (7).

Two other modifications were made to improve the stability and robustness of the algorithm. First,

the magnitudes of the minimum allowable k and ϵ values were reduced in order to obtain acceptable turbulence profiles within the sublayer region. Use of higher values, such as those used in the original Chien $k-\epsilon$ implementation, were found to artificially impose the turbulent time scale $\tau_T = k/\epsilon$ very near the wall. Second, the implicit treatment of the source terms was modified to improve the diagonal dominance of the system.

Modifications were also made to the WIND post-processing tool, CFPOST, to allow for the examination and extraction of the turbulent stresses from the solution files.

Results

The ASM results presented below are compared with those obtained using the Shear Stress Transport (SST)[14] and Chien[17] $k-\epsilon$ two-equation turbulence models, which utilize the Boussinesq approximation. The SST model is a two-layer model, where the $k-\omega$ model of Wilcox[18] is used in the near-wall region and the high Reynolds number $k-\epsilon$ model of Jones-Launder[19] is used in the outer region of the boundary layer and away from walls. A blending function is used to facilitate the switch between the two layers. The SST model is widely used because of its robustness and versatility. The Chien model is representative of the $k-\epsilon$ models and can be numerically integrated through viscous wall regions. Again, no explicit compressibility corrections, such as those for pressure dilatation or dilatation dissipation, have been used with any of the turbulence models investigated.

Flat Plate

The incompressible flow over a smooth flat plate, originally reported by Wieghardt[20] and later included in the compilation of reference 21, was chosen as an initial validation case for two reasons. First, this benchmark flow can be used to ascertain the integrity of the WIND ASM $k-\epsilon$ implementation without the added complexity of compressibility effects, which the present model does not specifically account for. Second, this case has been used to validate many of the other turbulence models in WIND and therefore provides a basis for comparing computational issues such as grid sensitivity.

A Cartesian mesh with 111 points in the axial direction and 81 points normal to the viscous wall was used. The first 14 axial points upstream of the leading edge of the plate were treated as an inviscid wall to provide a uniform profile at the leading edge location. The mesh was clustered in the streamwise direction to resolve flow gradients near the leading edge of the plate and normal to the surface to resolve the boundary layer. Calculations were made on a series of grids having a nominal y^+ values of 1, 2, and 5 at the first point off the wall. In a previous study[16] these values were shown to be representative of the maximum y^+ along the the plate. The freestream Mach number in the simulations was set to 0.20, slightly higher than in the experiment, in order to accelerate the convergence rate of the code.

Based on skin friction results, the grid dependence of the ASM was found to be comparable to that of the Chien $k-\epsilon$ model. Both models exhibited only minor differences between solutions obtained on the $y^+ = 1$ and $y^+ = 2$ grids. However, the error in the ASM predictions was found to increase to 20 percent when using the $y^+ = 5$ mesh. For the Chien $k-\epsilon$ model, the error was roughly 10 percent. This grid sensitivity is decidedly more pronounced than observed in the previous validation of the Chien $k-\epsilon$ model[16] and is likely due to reducing the minimum allowable values of the turbulence variables. It is generally recommended that one place the first grid point deep within the sublayer, usually at or below $y^+ \approx 1$. All of the results that follow are those obtained on the $y^+ = 1$ mesh.

Figure 1 shows the skin friction distribution along the flat plate. The ASM and $k-\epsilon$ results are in very close agreement with each other, while the SST results are slightly lower. All of the solutions are within 1 to 2 percent of the experimental data. Velocity profiles at the $Re_x = 4.2\text{x}10^6$ location are given in Figure 2. All of the models provide satisfactory results.

Turbulent kinetic energy profiles are shown in Figure 3 with the "average" experimental data compiled by Patel, Rodi, and Scheuerer.[22] The SST and ASM results are very similar and fail to predict the peak in k that is located around $y^+ = 15$. This occurs because neither model contains the near-wall terms needed capture this feature of the flow. The Chien $k-\epsilon$ model does contain these terms and provides better agreement with the data in this regard.

All of the models reasonably predict the turbulent shear stress in both the inner (Figure 4) and outer (Figure 5) parts of the boundary layer. Turbulence intensity profiles are shown in Figure 6. Both the SST and $k-\epsilon$ models, which use the Boussinesq approximation, predict an equal partition of the turbulent kinetic energy between the three components. The ASM does not rely upon the Boussinesq approximation and predicts $\overline{v''v''} < \overline{w''w''} < \overline{u''u''}$, which is in agreement with the data. However, the model's lack of near-wall terms to capture the peak in turbulent kinetic energy

also prevents the model from predicting the sharp rise in turbulence intensities very near the wall.

Mixing Layer

The second case to be examined is the compressible planar shear layer, identified as case 2 by Goebel and Dutton.[23] In this flow, two parallel supersonic streams, which are initially separated by a splitter plate, are allowed to interact to form a shear layer. At the entrance of the mixing region, the flow conditions for the high-speed stream are reported to be M=1.91, T_t=578 °K, and U=700 m/s. Those for the low-speed stream are M=1.36, T_t=295 °K, and U=399 m/s. The two streams are reportedly pressure-matched at 49 kPa. The convective Mach number for this case, based upon these flow conditions, is 0.46.

This problem was modeled using three zones. The first two zones, each 101x101, were used to model the growth of the upstream boundary layers on either edge of the splitter plate. The high-speed stream required an upstream extent of 240 mm in order to match the momentum thickness measured in the experiment near the end of the plate. Similarly, the low-speed stream required 160 mm. The third zone, 401x241 in size, was used to model the 500 mm by 48 mm mixing region. Forty-one points were placed across the base region of the splitter plate which was 0.5 mm thick. The grid was clustered vertically to capture the boundary layers and the shear layer. It was also clustered axially towards the splitter plate trailing edge to resolve the initial development region of the shear layer. The y^+ values over the majority of the domain varied between 0.8 and 1.0. In the experiment, the upper and lower walls of the mixing section were angled to accomodate the growth of the boundary layers. For the computations, straight-walled inviscid boundaries were used. Results obtained using this grid sequenced one level (i.e., every other point) in both directions were nearly identical to those obtained using the full grid.

Figure 7 compares the mean velocity profiles at several axial stations throughout the mixing region. At the entrance to the mixing region, all of the results are nearly identical and agree very well with the experimental data. Further downstream, there is still very little difference between the SST and $k-\epsilon$ model results, as one would expect for a free shear flow such as this. These results can very nearly be represented as a linear interpolation between either core stream velocity. That is to say that these velocity profiles exhibit a nearly linear slope which abruptly changes at either edge of the shear layer. The ASM profile results, on the other hand, have a distinctive non-linear shape which appears to be more in line with that exhibited by the experimental data.

Profiles of the streamwise and transverse turbulence intensities are shown in Figures 8 and 9. As with the boundary layer results, the SST and $k-\epsilon$ models again predict a nearly equal partition of k between these two normal stresses. The ASM much more accurately predicts the higher values of streamwise intensity and lower values of transverse intensity indicated by the data. Profiles of spanwise turbulence intensity are not shown, due to lack of experimental data. However, the predicted ASM profiles are similar in shape to those shown in Figures 8 and 9, with peak values that are not quite midway between those for the streamwise and transeverse intensities. Profiles of the turbulent shear stress given in Figure 10 also appear to indicate the superiority of the ASM over the SST and $k-\epsilon$ models, particularly in the initial development region.

Figure 11 compares the shear layer thickness b, which is defined as the distance between transverse locations where $\widetilde{u} = \widetilde{u}_1 - 0.1\Delta\widetilde{u}$ and $\widetilde{u} = \widetilde{u}_2 + 0.1\Delta\widetilde{u}$. The ASM is observed to predict a shear layer which is roughly 20 percent thinner than that of the SST or $k-\epsilon$ models. Refering back to the velocity profiles given in Figure 7, one can clearly see that the width of the shear layer predicted with the ASM is in fact smaller. Even if the models were identical in their predictions of the shear layer edge locations, the ASM would still yield a smaller shear layer thickness based on the 10 percent $\Delta\widetilde{u}$ criteria, due to the non-linear shape of the ASM profiles.

With regards to the experimental data, the ASM is in excellent agreement within the first half of the mixing region. Further downstream, the model underpredicts the shear layer thickness. The SST and $k-\epsilon$ models predict a much more rapid growth in the region from x =75 mm to x =225 mm, but tend to provide slightly better agreement further downstream. The mixing layer growth rate, db/dx, is often used as a quantitative measure of model performance. Table 1 summarizes the values obtained in this investigation. These are computed using a linear least-squares fit of the CFD at the experimental profile locations between 100 mm and 450 mm, the self-similar region reported in the experiment. Based on these values alone, one would likely conclude that the $k-\epsilon$ model performs the best. However, the profile plots indicate that the ASM holds distinct advantages over the two-equation models.

	db/dx
Goebel	0.0381
SST	0.0392
$k-\epsilon$	0.0379
ASM $k-\epsilon$	0.0295

Table 1: Mixing Layer Growth Rates

Elliptic Nozzle

The final case to be examined is the elliptic nozzle tested experimentally by Seiner and Ponton.[24] As illustrated in Figure 12 this nozzle has an aspect ratio (major axis diameter divided by minor axis diameter) of 2 and an exit area of 1.571 in^2. At the exit plane, the nozzle wall was 0.02 inches thick. The nozzle was operated at a total temperature of 564 °R and a nozzle pressure ratio (nozzle total pressure divided by freestream static pressure) of 3.67. This provided a design exit Mach number of 1.52.

Due to the symmetry of the geometry, only a 90° section from the major axis to the minor axis was modeled. The grid for this case was divided into three zones. The mesh for the internal nozzle region contained 87 points in the axial direction and 61 points in the radial direction. The zone used to model the freestream inflow region contained 61 axial and 61 radial points. These two zones were point-to-point matched with a 101x151 zone used to model the downstream plume region, which extended 100 inches. This left 29 points in the radial direction to resolve the base region downstream of the nozzle lip. In each zone, 46 points were used in the circumferential direction. The y^+ values along the interior nozzle wall were less than one.

The operating conditions described above were used to set the inflow conditions for the calculations. In order to prevent convergence difficulties, the ambient air was modeled as having a freestream Mach number of 0.07. WIND was run in 100 cycle intervals at 5 iterations per cycle with a CFL number of 1.5. Solutions were deemed converged when the maximum percent change in the centerline velocity between two successive solutions dropped below 0.01 percent.

Figure 13 compares the centerline velocity decay of the jet. For this case, the $k-\epsilon$ model has the highest initial rate of jet mixing, as indicated by the length of the potential core, followed by the SST model and the ASM. Relative to the data, the $k-\epsilon$ model most accurately predicts the core length. Further downstream, all of the models decay at a slightly faster rate than indicated by the data.

Mean velocity profiles along the major and minor axes are presented in Figure 14 at several axial locations. The $k-\epsilon$ and SST models yield similar, though not identical, results. Both predict a shear layer which is thinner than experiment along the major axis and thicker than experiment along the minor axis. These calculations therefore predict a jet which becomes much more round compared to the data. These findings were previously reported by Georgiadis,[25] who speculated that the inability of these models to accurately represent the three-dimensional effects of this elliptic jet may be linked to their isotropic nature. The ASM results for this case appear to support that premise. The major axis profiles illustrate a considerable improvement over the two-equation results. The minor axis profiles also show improvement. The only major difficiency in the ASM results appears to be in the centerline decay. Therefore one must recognize that solely using the centerline velocity decay as an indicator of the ability of these turbulence models will lead to the incorrect conclusion that the two-equation models are not only adequate, but superior, for this type of flow.

Turbulence intensity profiles are presented in Figure 15. The $k-\epsilon$ and SST results once again predict a nearly isotropic distribution, while the ASM clearly displays anisotropy. The turbulence intensity in the streamwise direction is considerably larger than in the other two directions. It is also interesting to note that along the major (z=0) axis $\overline{v''v''} < \overline{w''w''}$, while along the minor (y=0) axis this trend is reversed. This is consistent with the planar mixing layer results in that the turbulence intensity in the dominant shear direction (the y-direction for that case) was found to be the smallest. Along the major axis the dominant velocity gradient is in the y-direction, while along the minor axis the gradient is in the z-direction. Unfortunately, no turbulence statistics are available from the experiment to confirm this behavior.

Conclusions and Future Work

An incompressible algebraic Reynolds stress turbulence model has been implemented in the WIND Navier-Stokes flow solver and has been thoroughly validated for an incompressible boundary layer. The model was then applied to a compressible planar mixing layer and a supersonic elliptic jet. In all of these calculations, the ASM demonstrated its unique ability to predict anisotropy among the Reynolds normal stresses. For the mixing layer calculation, the ASM was found to more accurately predict the shape of the mean velocity profiles and the turbulent stresses relative to two-equation eddy viscosity models, but slightly underpredicted the

shear layer growth rate. For the elliptic jet, the ASM results for the mean velocity profiles along the major and minor axes were in much better agreement with experimental observations. The linear two-equation models tended to predict a much more round-like jet. However, in examining the centerline mean velocity decay, the ASM was found to once again underpredict the amount of mixing.

These results suggest that it may be necessary to adjust some of the model coefficients in order to increase the rate of mixing predicted by the ASM. However, experience with two-equation models has indicated that one must be careful in this regard, since the amount of recalibration needed often depends on the level of compressibility of the flow. Future work shall focus first on determining the ASM's sensitivity to compressibility effects, then on evaluating various modifications for compressible flow. Model terms for the deviatoric pressure strain correlation tensor and the pressure dilatation will likely play a key role, as these correlation terms involve the fluctuating pressure.

Acknowledgments

This work was funded under the Aerospace Propulsion and Power, Research & Technology Base Program at the NASA Glenn Research Center. The author would like to express his gratitude to Dr. Christopher Rumsey of the NASA Langley Research Center for kindly sharing his expertise in implementing algebraic stress models in the CFL3D code.

References

1. Barber, T., Chiappetta, L., Debonis, J., Georgiadis, N., and Yoder, D., "Assessment of Parameters Influencing the Prediction of Shear-Layer Mixing," *Journal of Propulsion and Power*, Vol. 15, No. 1, 1999, pp. 45–53.

2. Khavaran, A. and Krejsa, E., "On the Role of Anisotropy in Turbulent Mixing Noise," AIAA Paper 98–2289, Jun. 1998.

3. Speziale, C. G., "Comparison of Explicit and Implicit Algebraic Stress Models of Turbulence," *AIAA Journal*, Vol. 35, No. 9, Sept. 1997, pp. 1506–1509.

4. Rodi, W., "A New Algebraic Relation for Calculating the Reynolds Stresses," *Z. Ang. Math. Mech.*, Vol. 56, 1976, pp. T219–T221.

5. Pope, S., "A More Effective Viscosity Hypothesis," *Journal of Fluid Mechanics*, Vol. 72, 1975, pp. 331–340.

6. Gatski, T. B. and Speziale, C. G., "On Explicit Algebraic Stress Models for Complex Turbulent Flows," *Journal of Fluid Mechanics*, Vol. 254, 1993, pp. 59–78.

7. Girimaji, S., "Fully-Explicit and Self-Consistent Algebraic Reynolds Stress Model," ICASE 95–82, 1995.

8. Jongen, T. and Gatski, T., "A Unified Analysis of Planar Homogeneous Turbulence Using Single-Point Closure Equations," *Journal of Fluid Mechanics*, Vol. 399, 1999, pp. 117–150.

9. Rumsey, C., Gatski, T., and Morrison, J., "Turbulence Model Predictions of Strongly Curved Flow in a U-Duct," *AIAA Journal*, Vol. 38, No. 8, Aug. 2000, pp. 1394–1402, Presented as AIAA Paper 99–0157.

10. Rumsey, C. and Gatski, T., "Recent Turbulence Model Advances Applied to Multielement Airfoil Computations," *Journal of Aircraft*, Vol. 38, No. 5, Sept. 2001, pp. 904–910, Presented as AIAA Paper 2000–4323.

11. Bush, R. H., Power, G. D., and Towne, C. E., "WIND: The Production Flow Solver of the NPARC Alliance," AIAA Paper 98–0935, Jan. 1998.

12. Nelson, C. and Power, G., "CHSSI Project CFD-7: The NPARC Alliance Flow Simulation System," AIAA Paper 2001–0594, Jan. 2001.

13. Wilcox, D. C., *Turbulence Modeling for CFD*, DCW Industries, 2nd ed., 1998.

14. Menter, F. R., "Two-Equation Eddy-Viscosity Turbulence Models for Engineering Applications," *AIAA Journal*, Vol. 32, No. 8, Aug. 1994, pp. 1598–1605, Presented as AIAA Paper 93–2906.

15. Speziale, C. G., Sarkar, S., and Gatski, T. B., "Modelling the Pressure-Strain Correlation of Turbulence: An Invarient Dynamical Systems Approach," *Journal of Fluid Mechanics*, Vol. 227, 1991, pp. 245–272.

16. Yoder, D. A. and Georgiadis, N. J., "Implementation and Validation of the Chien $k-\epsilon$ Turbulence Model in the WIND Navier-Stokes Code," NASA TM–1999–209080, Apr. 1999, See also AIAA Paper 99-0745.

17. Chien, K.-Y., "Predictions of Channel and Boundary-Layer Flows with a Low Reynolds

Number Turbulence Model," *AIAA Journal*, Vol. 20, No. 1, Jan. 1982, pp. 33–38.

18. Wilcox, D., "Reassessment of the Scale-Determining Equation for Advanced Turbulence Models," *AIAA Journal*, Vol. 26, No. 11, Nov. 1988, pp. 1299–1310.

19. Jones, W. and Launder, B., "The Calculation of Low-Reynolds-Number-Phenomena with a Two-Equation Model of Turbulence," *International Journal of Heat and Mass Transfer*, Vol. 16, 1973, pp. 1119–1130.

20. Wieghardt, K. and Tillmann, W., "On the Turbulent Friction Layer for Rising Pressure," NACA TM–1314, 1951.

21. Coles, D. E. and Hirst, E. A., editors, *Computation of Turbulent Boundary Layers-1968 AFOSR-IFP-Stanford Conference*, Vol. 2, Stanford University, CA, 1969.

22. Patel, V. C., Rodi, W., and Scheuerer, G., "Turbulence Models for Near-Wall and Low-Reynolds Number Flows: A Review," *AIAA Journal*, Vol. 23, No. 9, Sept. 1985, pp. 1308–1319.

23. Goebel, S. and Dutton, J., "Experimental Study of Compressible Turbulent Mixing Layers," *AIAA Journal*, Vol. 29, No. 4, Apr. 1991, pp. 538–546.

24. Seiner, J. and Ponton, M., "Supersonic Acoustic Source Mechanisms for Free Jets of Various Geometries," *AGARD 78th Specialists Meeting on Combat Aircraft Noise*, Bonn, Germany, Oct. 1991.

25. Georgiadis, N. J., Yoder, D. A., and DeBonis, J. R., "A Comparison of Three Navier-Stokes Solvers for Exhaust Nozzle Flowfields," AIAA Paper 99–0748, Jan. 1999.

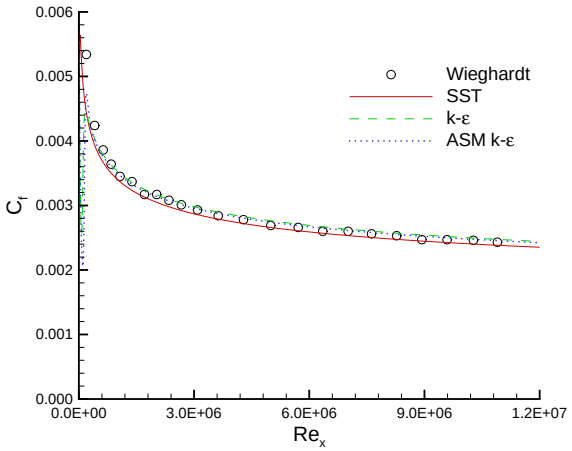

Figure 1: Flat Plate Skin Friction Results.

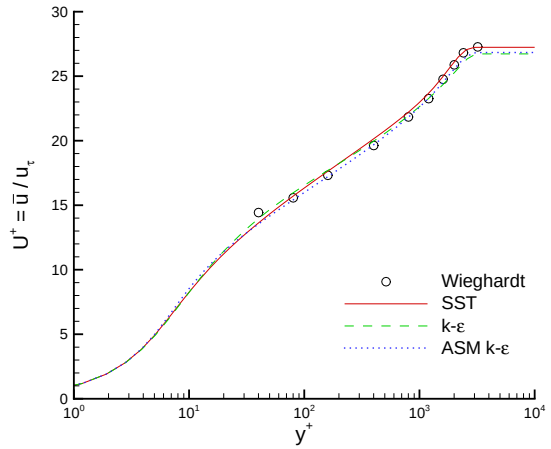

Figure 2: Flat Plate Velocity Profiles.

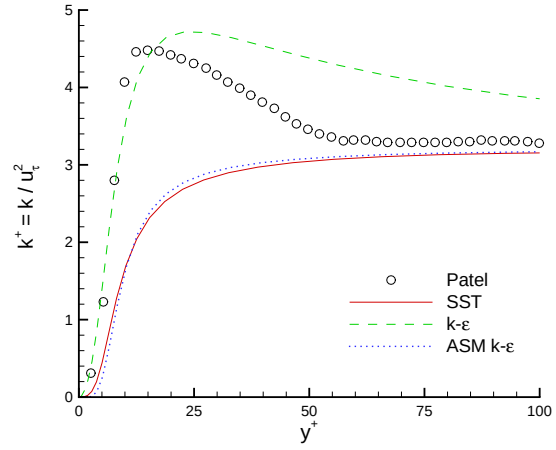

Figure 3: Flat Plate Turbulent Kinetic Energy Profiles.

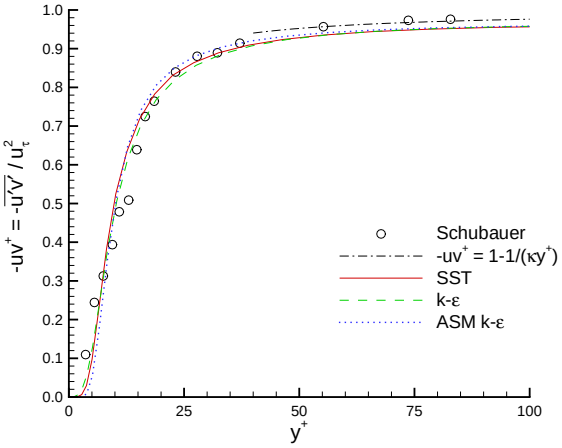

Figure 4: Flat Plate Turbulent Shear Stress Profiles.

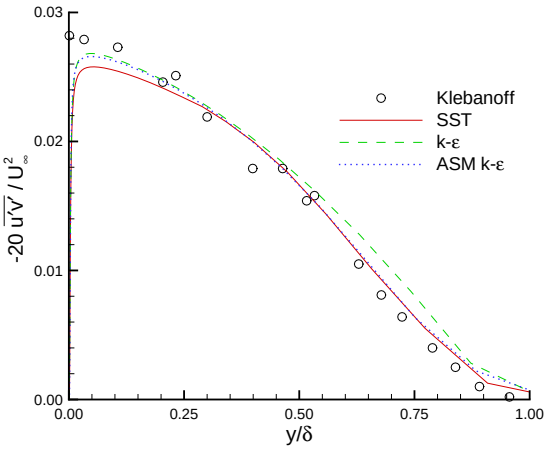

Figure 5: Flat Plate Turbulent Shear Stress Profiles in Outer-Layer Variables.

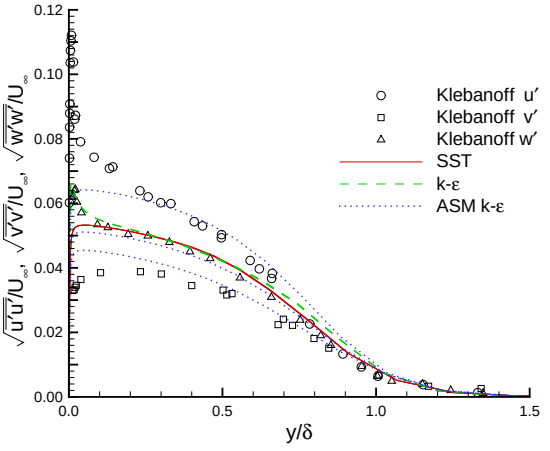

Figure 6: Flat Plate Turbulence Intensity Profiles in Outer-Layer Variables.

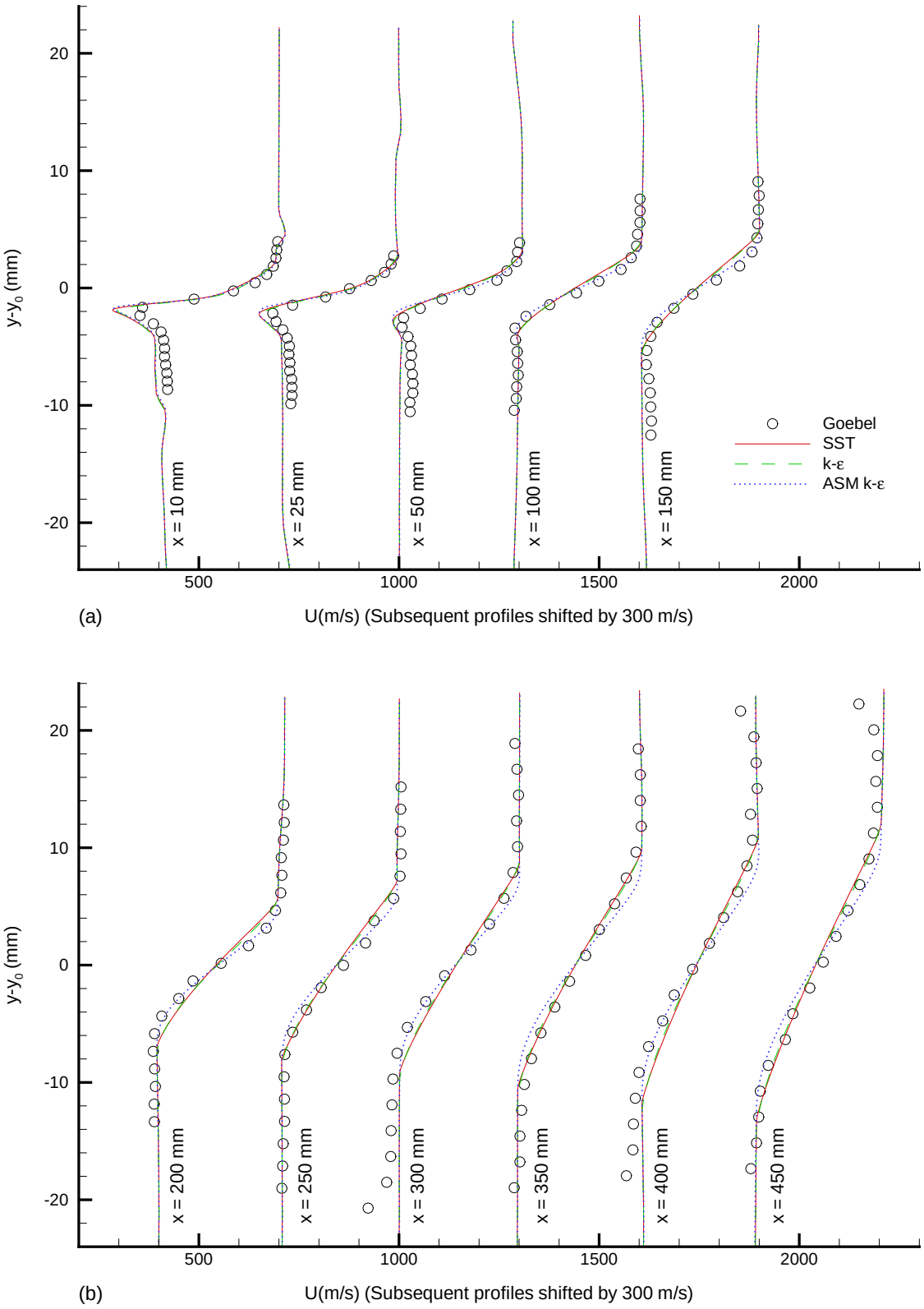

Figure 7: Planar Mixing Layer Velocity Profiles.

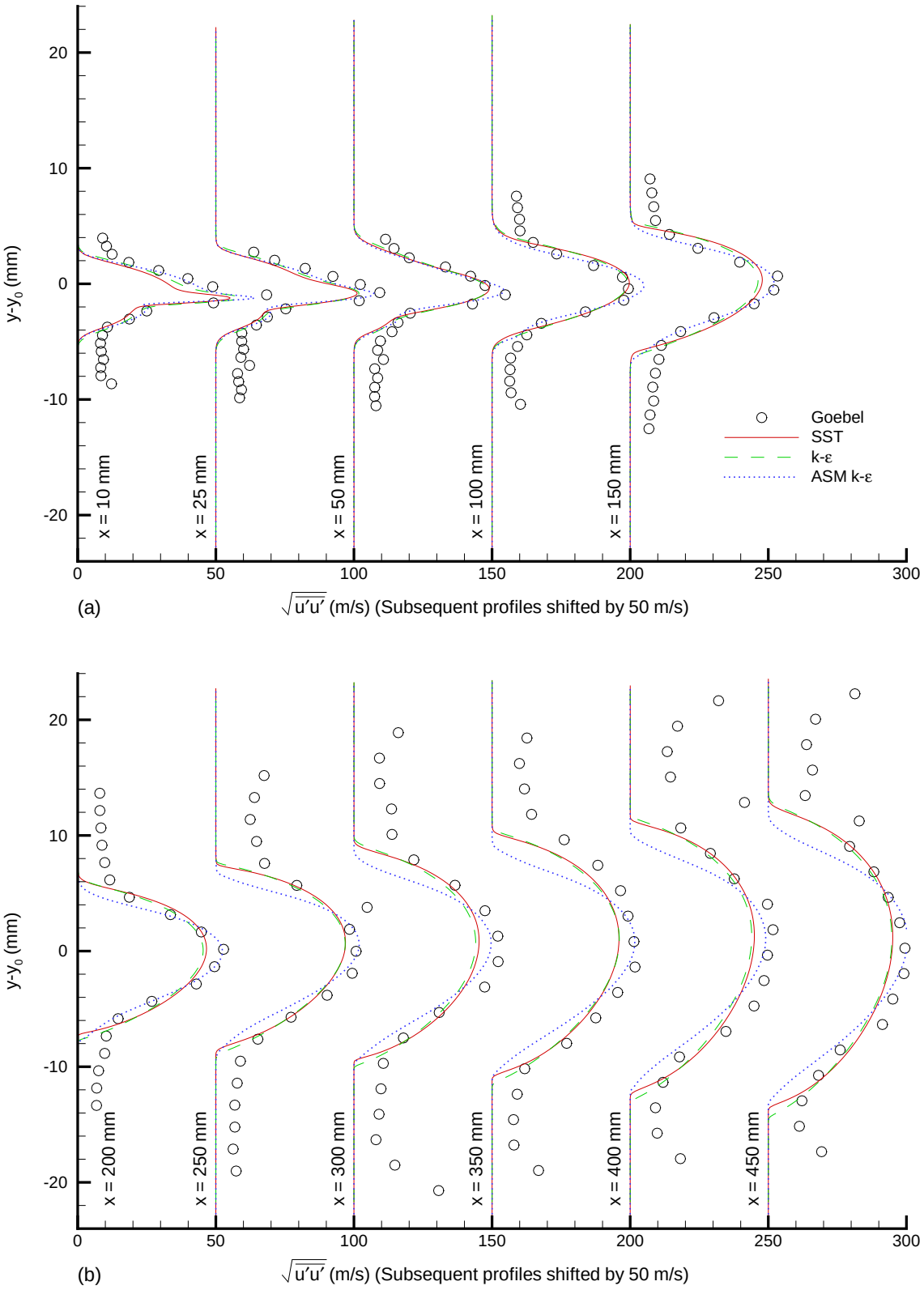

Figure 8: Planar Mixing Layer Streamwise Turbulence Intensity Profiles.

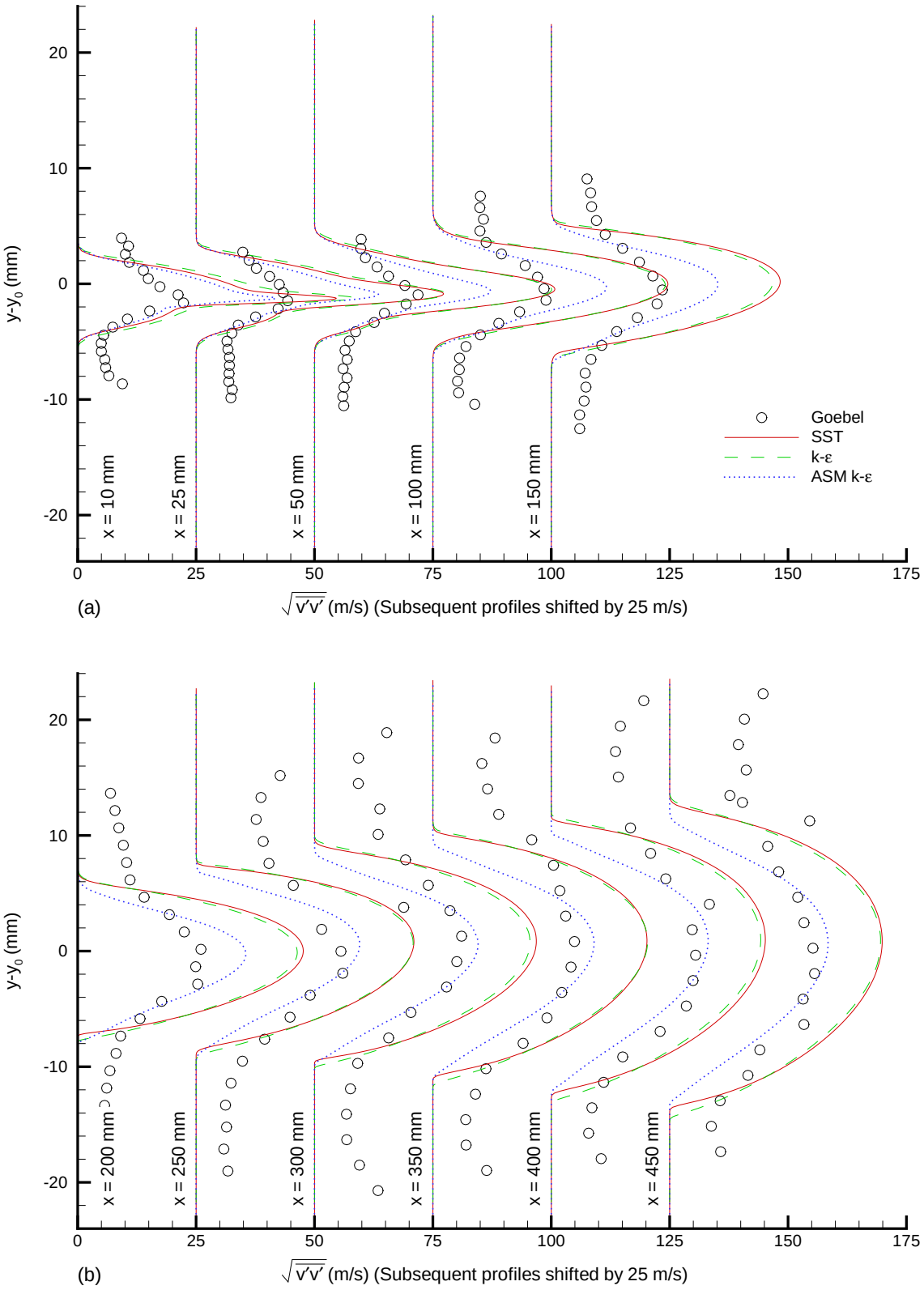

Figure 9: Planar Mixing Layer Transverse Turbulence Intensity Profiles.

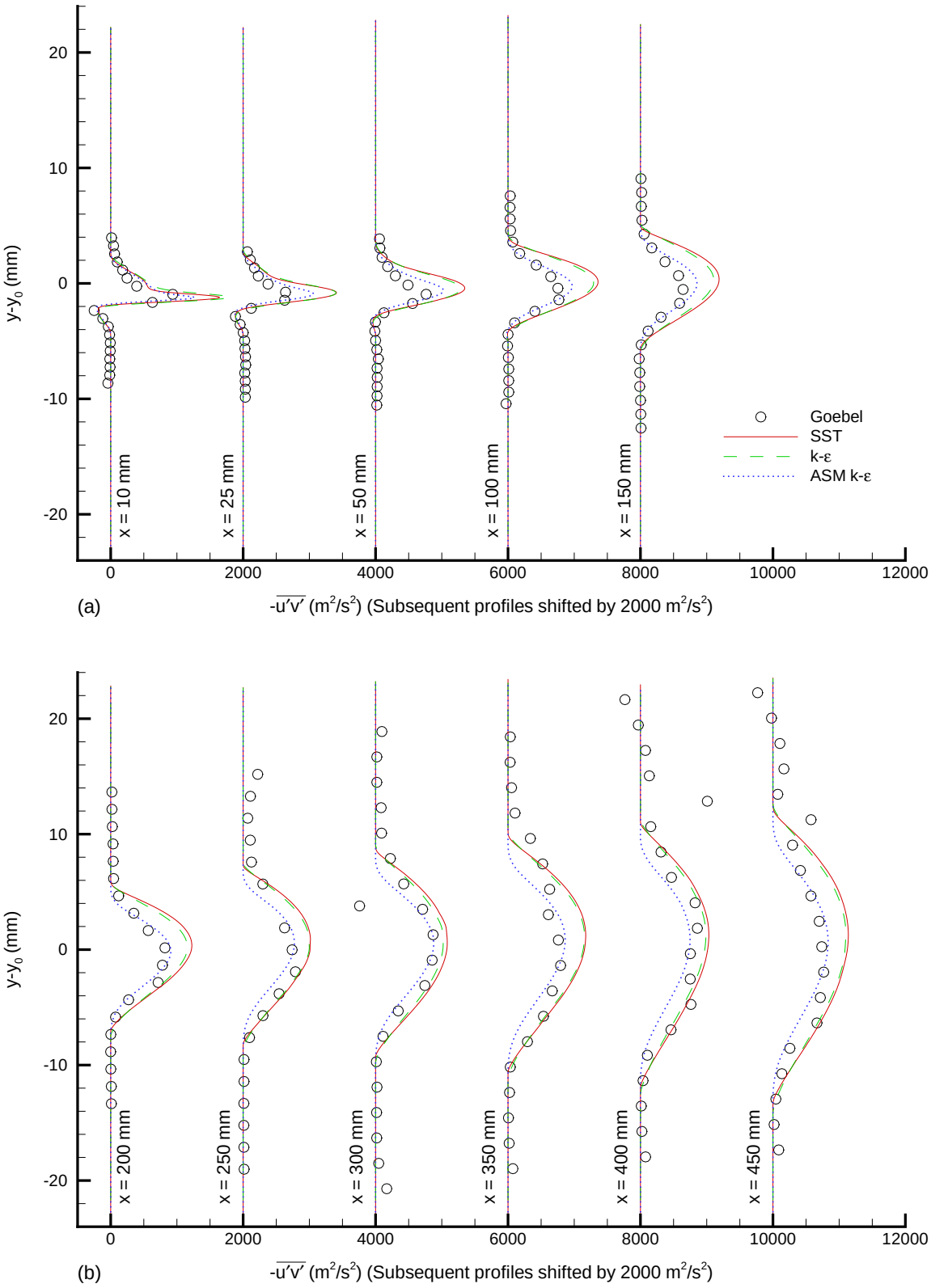

Figure 10: Planar Mixing Layer Turbulent Shear Stress Profiles.

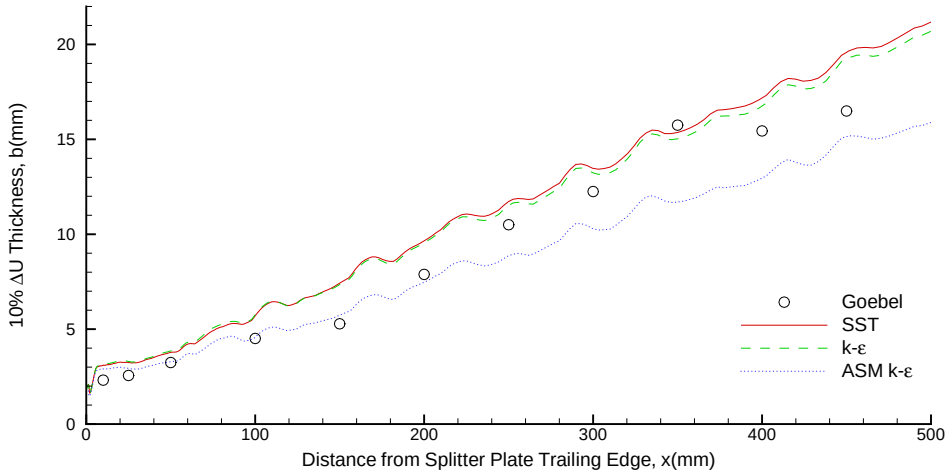

Figure 11: Planar Mixing Layer Shear Layer Thicknesses.

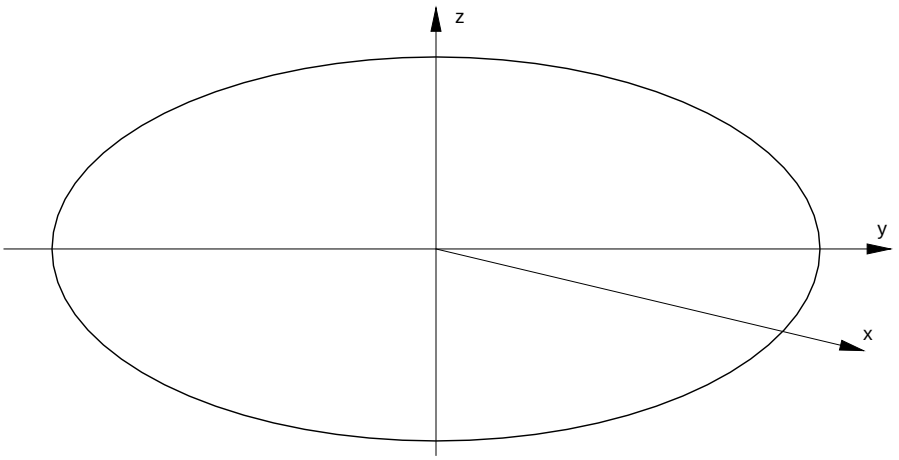

Figure 12: Schematic of Elliptic Nozzle Coordinate System.

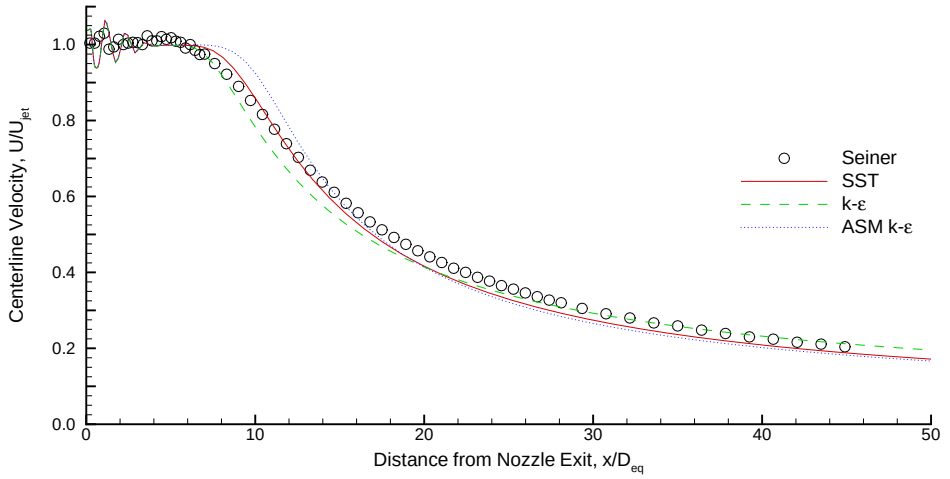

Figure 13: Elliptic Nozzle Centerline Velocity Decay.

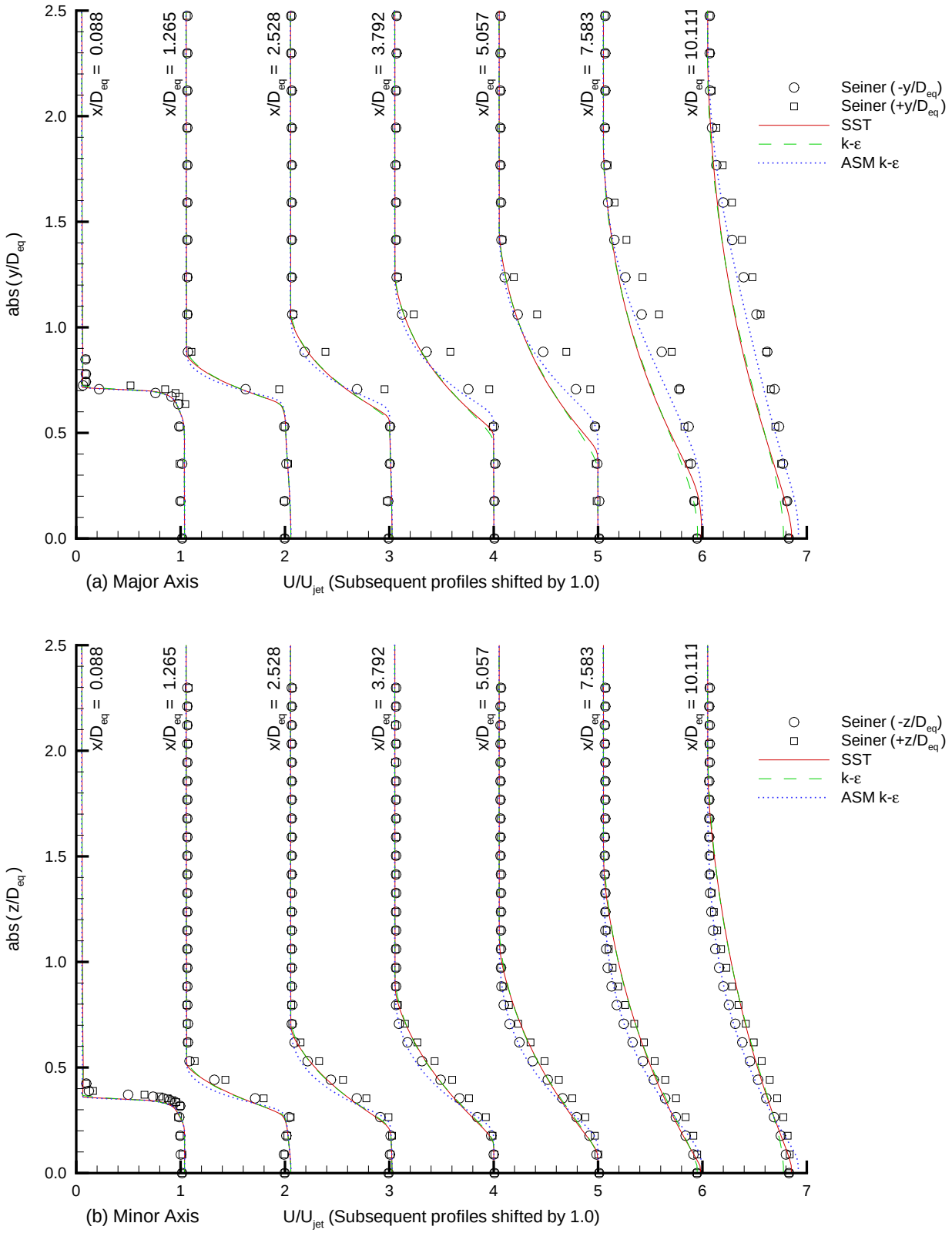

Figure 14: Elliptic Nozzle Mean Velocity Profiles.

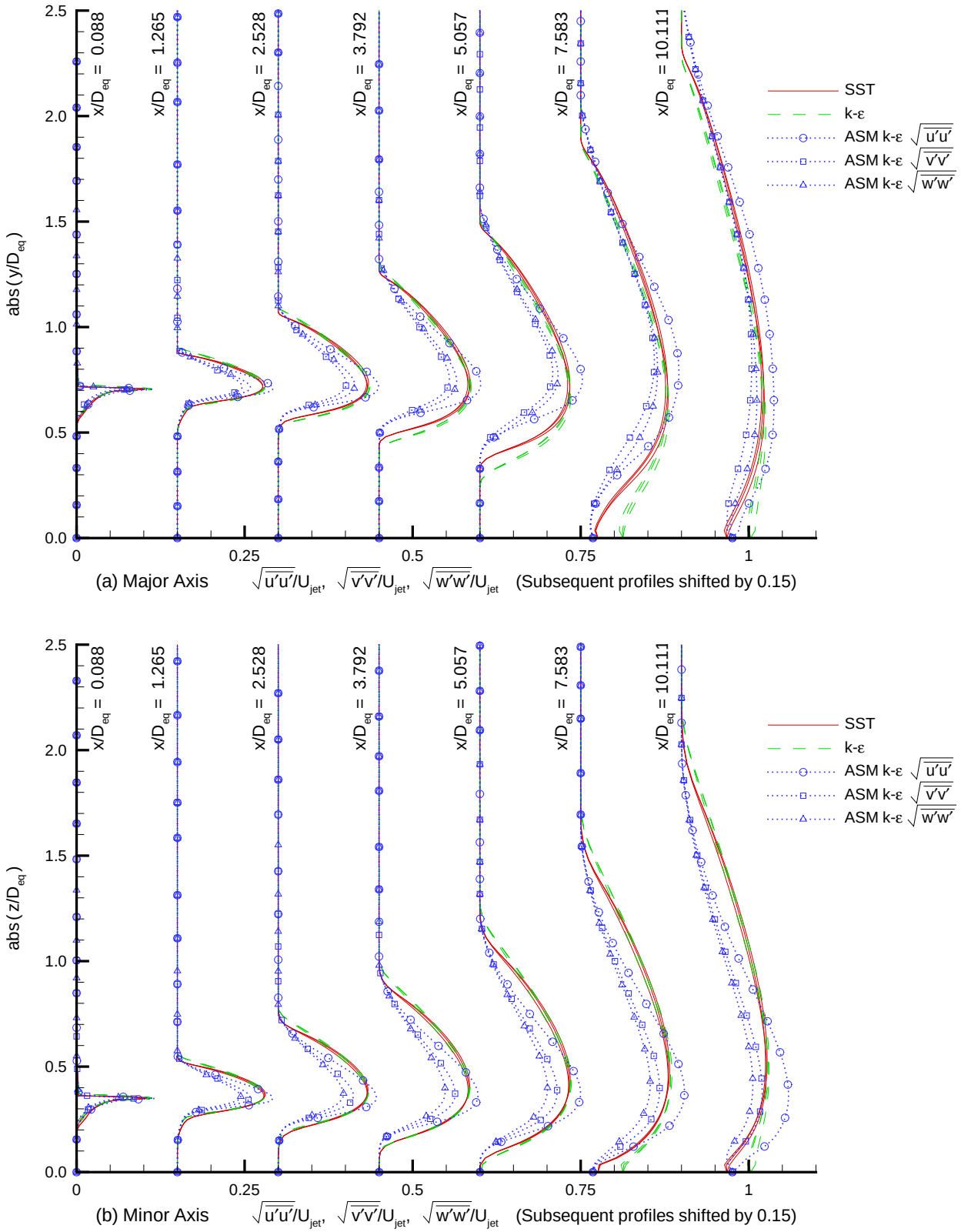

Figure 15: Elliptic Nozzle Turbulence Intensity Profiles.